

International Conference on Space Optics—ICSO 2018

Chania, Greece

9–12 October 2018

Edited by Zoran Sodnik, Nikos Karafolas, and Bruno Cugny



Photonic integrated circuits for ultra-fast steering in phased-array antennas

Francesco Amato

Giovanni Serafino

Filippo Scotti

Bilal Hussain

et al.



icso proceedings



Photonic Integrated Circuits for Ultra-fast Steering in Phased-Array Antennas

Francesco Amato^a, Giovanni Serafino^a, Filippo Scotti^{*b}, Bilal Hussain^b, Veronica Toccafondo^b,
Marco Chiesa^b, Claudio Porzi^a, Antonella Bogoni^{a,b}, Paolo Ghelfi^b

^aScuola Superiore Sant'Anna – TeCIP institute, Via Moruzzi 1, 56124 Pisa, Italy

^bCNIT – National Photonic Networks Laboratory, Via Moruzzi 1, 56124 Pisa, Italy

ABSTRACT

We report the design and implementation of a beam-forming network based on packaged integrated photonic circuits. Each of the four PICs emulating a phased-array antenna is optically fed by the 13GHz signal, and is able to adjust the phase exceeding 360° with a precision $<1^\circ$. Experiments demonstrate an ultrafast antenna reconfiguration in less than 5ns.

Keywords: Beam Forming Network, Photonic Integrated Circuit, Microwave Photonics

1. INTRODUCTION

The envisioned next generation satellite communication networks will guarantee high throughput to the users, relying on the increased bandwidth available at higher frequencies, ranging from the Ku-band in the proposed OneWeb constellation, up to the V-band that is considered by the StarLink constellation.

In fact, in the crowded RF spectrum, the higher frequencies are less utilized; Moreover they are very attractive due to the potentially available bandwidth. On the other hand, these frequencies experience high propagation losses, thus their exploitation requires transceivers with an increased power and high gain antennas. Both these solutions are hard to be implemented: increasing the power also makes the size, weight, and power consumption growing, while high gain antennas present a reduced illuminating area, thus a limited number of potential users to be served. To overcome these limitations, operators are designing huge constellations of several hundred satellites, each serving a small portion of the surface. Moreover, also to limit the distance from the users, these satellites will operate in low Earth orbit rather than geostationary orbit, thus the user will be required to actively track the satellite motion through the sky. In fact, both OneWeb and StarLink require the user employing Phased Array Antennas (PAAs) with sizes of about 40cm. This approach is limited to fixed users and it can't be applied for mobile applications due to the antenna dimensions. To further increase the link gain, user-specific beamforming (BF) will play a key role. In the next-future wireless communications scenario, beamforming networks (BFNs) are expected to drive PAAs with potentially several elements, whose size will shrink due to the employed high frequency. Therefore, antenna pointing accuracy, low losses, reduced power consumption, and small size are crucial characteristics in future BFNs. Moreover, to efficiently track multiple users from a fast moving satellite, the steering velocity will be crucial.

In this perspective, photonics can provide promising solutions to meet these requirements. In fact, the requisites of increased bandwidth and carrier frequency of signals are very demanding for present-day digital RF phase shifters (PSs), which exhibit important insertion loss and power consumption, together with non-negligible phase errors. Optical phase shifter instead presents a good linearity, and can be easily employed together with the almost-lossless optical distribution of signals for antenna remoting.

Among the different proposed techniques, solutions based on photonic integrated circuits (PICs) distinguished as the most promising approach for practical PS implementation based on microwave photonics, due to increased stability, drastically minimized size and weight, and possibility of low operating power. By resorting to different technological platforms, several PICs have been realized in the last years to implement microwave PS operation. Largely exploited techniques in order to control the phase of a microwave signal in the optical domain are based on the exploitation of the

thermo-optic effect in silica [1], silicon [2][3], and Si_3N_4 [4] microring resonators (MRRs). Thermal effects are however slow, and typically hinder operations above ~ 100 kHz. The silicon on insulator (SOI) technological platform, which notably permits to realize PICs with a CMOS-compatible process, also allows to exploit the free-carrier modulation effect [5], as a much faster mean (albeit weaker and with higher loss) than thermo-optic effect for controlling the phase of an optical signal.

In this work, we report a complete photonics-based beamforming network demonstration for a 4-element PAA, based on a packaged PIC, operated in an electronic printed circuit board (PCB). The PICs are realized in SOI technology which simultaneously matches the demand for wide phase-shift range, broad bandwidth, low in-band power oscillations, fast reconfiguration speed, and compatibility with CMOS integrated circuits fabrication technology. The PICs are able to perform stable phase shifts well in excess of 360° over a bandwidth of 6 GHz for RF carriers spanning in the X, Ku, an mm-wave bands, with a response time below 1 ns.

2. PHOTONIC INTEGRATED PHASE SHIFTER CIRCUIT

2.1 PIC operation principle and design

The operation principle of the proposed photonics-based PS is illustrated in Fig. 1(a). The core element of the architecture, realized as a PIC, is highlighted in the dashed box of the figure and comprises an optical deinterleaver filter (ODF), an optical phase shifter (OPS), an optical coupler (OC), and finally two photodiodes (PDs). The input of the scheme is represented by the microwave signal to be phase-shifted, with a given bandwidth around the carrier frequency f_{RF} , which drives a single-sideband electro-optic modulator (SSB-EOM) to generate a sideband centered at the optical frequency ν_{sb} , spaced by f_{RF} from the optical carrier at frequency ν_c provided by a laser source (LS). The generated full-carrier SSB modulated optical signal is then fed into the PS.

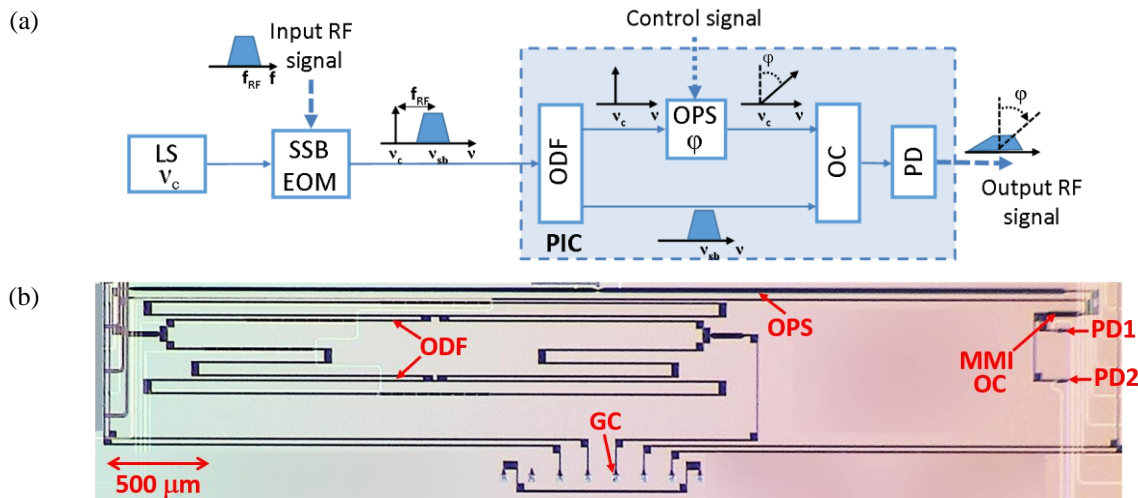


Figure 1. (a) Schematic and operation principle of the proposed photonic integrated phase shifter. LS: laser source; SSB EOM: single-sideband electro-optical modulator; ODF: optical deinterleaver filter; OPS: optical phase shifter; OC: optical coupler; PD: photodiode. In the scheme, f_{RF} represents the RF signal carrier frequency, ν_c optical carrier frequency, ν_{sb} central optical frequency of the optical SSB modulated signal, ϕ variable phase shift. (b) Picture of the fabricated PIC implementing the phase shifter; GC: grating coupler; MMI-OC: multi-mode interference optical coupler. Two PDs are connected to the two MMI outputs. As shown by the scale indication, the PIC occupies an area of $\sim 5 \times 2.4 \text{ mm}^2$.

The operation of the scheme relies on optical carrier-sideband separation performed by the ODF and subsequent phase shift of the isolated carrier in the OPS stage, before the two components are recombined in the OC and sent to the PDs to generate the phase-shifted microwave signal [6]. The phase of the down-converted signal at the PDs output generated by the beating between the carrier and the sideband components is indeed given by the phase difference of the two beating signals. Assuming a perfect carrier-sideband isolation at the ODF outputs, the amount of optical phase shift ϕ

experienced by the optical carrier in the OPS translates into an equal phase shift ϕ of the microwave signal at fRF, as depicted in Fig. 1(a).

The PIC implementing the scheme, has been designed and fabricated in SOI technology through a multi-project wafer run [7]. A microscope picture of the fabricated device is shown in Fig. 1(b). The coupling of the optical signals with the photonic circuit exploits grating couplers (GCs) and vertical coupling with the accessing optical fibers. The ODF is implemented by a MRR-loaded MZ interferometer [8]. The OPS element is realized in a 4.25 mm-long interdigitated p-n junction, embedded in a silicon rib waveguide. The desired phase shift is achieved by applying the proper reverse voltage to the junction, thus causing a variation in the extension of the depletion region. The corresponding change of the waveguide effective index allows for controlling the phase of the optical signal at the output of the OPS. A 2x2 multi-mode interference (MMI) OC recombines the phase-shifted optical carrier and the modulated sideband before the detection in germanium photodiodes, with a -3dB bandwidth of about 20GHz. In fact, by exploiting the two available phase-offset replica of the microwave signal, the PDs, have been connected to each output waveguide the 2x2 MMI. This has been done with the aim of realizing a the subsequent off-chip balanced configuration for the PDs on a printed circuit board, by properly connecting the ground and signal contacts of the PD pairs, which has the twofold advantage of a 6 dB improvement in the output RF power and common mode noise cancellation.

2.2 PIC characterization

The optical transmission spectrum of the ODF at one output port is depicted in Fig. 2 (a). A periodic box-like transmission is observed, exhibiting a flat passband with a -1 dB bandwidth of 10 GHz and steep roll-off. The free-spectral-range (FSR) is 26 GHz, whereas the -30 dB stop-band width is around 6.5 GHz. The frequency response of the fabricated PIC shows an almost perfect agreement with the simulated target design, where a value of ~ 1.7 dB/cm has been used for the propagation loss of the strip waveguides, as available from the photonic design kit of the technological process. At the other output of the ODF, the transmission spectrum is the complementary. The OPS has also been characterized on a test structure, by embedding it within a MZ interferometer and observing the power variations of the output optical signal from the interferometer as a function of the applied reverse bias to the p-n junction. The measured characteristic of the OPS is plotted in Fig. 2(b), where a linear 475° phase shift over a bias range of 8V for the p-n junction reverse bias reported, giving the considerable precision of $0.06^\circ/\text{mV}$.

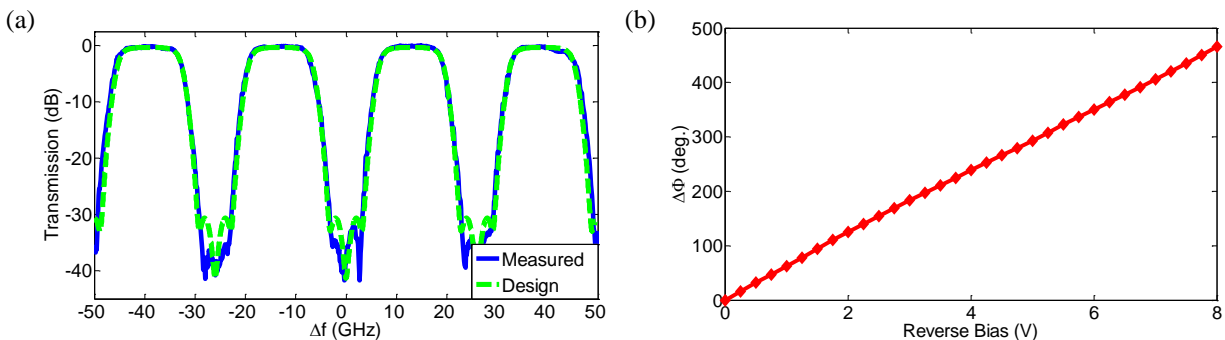


Figure 2. (a) Measured (solid blue) transmission spectrum of the ODF, and corresponding design simulation (dashed green) curves. The filter' free spectral range is 26GHz; the -1dB bandwidth is 10 GHz. (b) Measured relative phase shift $\Delta\phi$ vs. applied reverse bias to the p-n junction waveguide OPS.

For the characterization of the integrated circuit, a dual parallel MZ modulator (DPMZM) has been used to generate a full-carrier SSB modulated optical signal, then boosted by an erbium-doped fiber amplifier (EDFA) up to 10 dBm and finally injected into the PIC. Before entering the PIC, the optical signal passes through a polarization controller (PC) for maximizing the coupling efficiency of injected light with the fundamental TE mode of the silicon waveguides in the PIC through the GC. The optical carrier generated by the LS is tuned in the center of the ODF passband window by which it is routed towards the OPS branch of the PS (see Fig. 1(a)). To test the RF bandwidth of the proposed PS, the VNA has been operated in the sweep mode over a proper frequency range, so that the sideband optical frequency spanned across the ODF passband at the output port connected to the pass-through path. The photodetected microwave signal produced by carrier-sideband beating in the PDs is collected through an electrical probe and then sent back to the VNA for performance evaluation through magnitude and phase measurement of the S21 parameter.

In a first set of measurements, the output continuous-wave frequency from the VNA is swept over a bandwidth of 6 GHz around the central value of $f_{RF} = 13$ GHz. Therefore, the sideband of the full-carrier SSB modulated signal is swept over the transmission passband of the lower part of the ODF. The corresponding measurements on S21 parameters are reported in Fig. 3(a), where the phase of the S21 parameters over the considered frequency span is reported for different values of the bias voltage applied to the OPS. The curves of the phase response illustrate an almost flat phase shifts in the whole 6 GHz band, spanning over more than 450° , as the OPS control signal ranges between 0 and -8V. The standard deviation of the measured phase response in the full bandwidth range stays below 2° over a 360° phase shift.

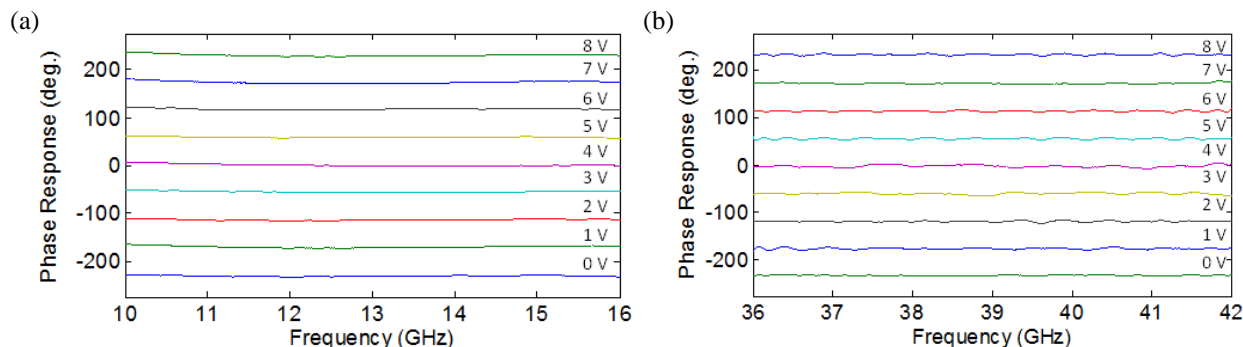


Figure 3. (a) Phase response of the MWP-PS, as a function of the RF frequency, over a 10-to-16 GHz frequency span. The phase response traces correspond to an applied bias voltages ranging (from top to bottom) between 0 and -8V with -1V steps. (b) Phase (bottom) response of the MWP-PS, as a function of the RF frequency, over a 36-to-42 GHz frequency span. The phase response traces correspond to an applied bias voltages ranging (from top to bottom) between 0 and -8V with -1V steps.

Similar characteristics have been observed by tuning the LS carrier frequency at the short- and long-frequency edge of the ODF passband, and performing a 6 GHz sweep around $f_{RF} = 10$ GHz and $f_{RF} = 16$ GHz, respectively, illustrating the potentials of the scheme for flexible operation with different RF carrier values. The periodic response of the ODF reported in Fig. 2, where the FSR of 26 GHz denotes the frequency spacing between consecutive passband windows, indicates that strong-rejection carrier-sideband isolation can be obtained around any RF carrier value that is an odd multiple of half the FSR. This property thus enables to suitably extend the operation of the device up to the mm-wave band. In order to demonstrate mm-wave band operation, the central value of the VNA frequency sweep has thus been set to $f_{RF} = 39$ GHz. Since the integrated germanium PDs in the PIC provided a very limited response at such frequencies, a test structure with a GC for optical output access after the MMI coupler has been used in conjunction with an external PD with -3dB bandwidth of 35 GHz. The results of the measurements, which have been performed in a similar manner as in the case of Fig. 3(a), are reported in Fig. 3(b), illustrating the potentials of the proposed scheme for broadband operation in the extremely high frequency (EHF) region. In the whole 8V voltage excursion, The measured maximum standard deviation of the phase is around 3.5° . These fluctuations are partially ascribed also to the increased sensitivity of both the reference and sample traces to noise oscillations due to the limited bandwidth of the available electrical equipment in the set-up.

3. PIC-BASED BEAM FORMING NETWORK

3.1 BFN design and implementation

Since a real beam forming network requires a phase shifting circuit for each antenna element, multiple PICs have to be used simultaneously and independently. In order to achieve this ability in a practical way, a dedicated electronic PCB housing the PICs has been designed and fabricated.

The realized PCB, shown in Fig. 4, hosts the PIC and assures the required DC biases as well as the thermal stabilization, and manages the balanced configuration of the PDs providing also the opportune amplification to obtain a single ended output with an RF power up to 0 dBm.

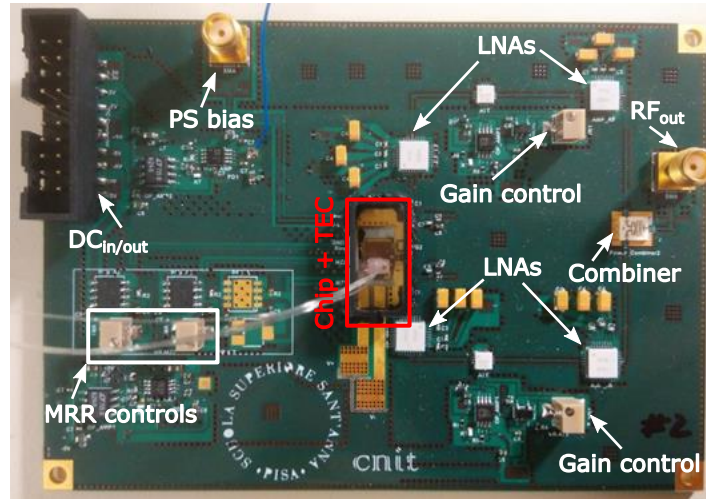


Figure 4. Top view of the manufactured beamforming microwave board. The photonic chip is in the center together with the TEC and the thermistor.

In details, the PIC is housed together with a thermo electric cooler (TEC) in a 5.5mm wide hole in the middle of the board, whose thickness of 1.6mm has been carefully selected to reduce the length of the wires bonding the PIC with the PCB, and thus their inductance which has been measured as low as 1.5nH.

The left-side of the board routes the DC and HF control signals used to properly bias the PIC, i.e. two trimmers to balance the upper and lower arms of the ODF, and a SMA connector to control externally apply the phase shift control. The right-side houses the RF components to amplify and recombine the RF signals upon transmission. The outputs of the PDs consist of two RF microwave signals of -40 dBm each and shifted by 160° from each other. The right side of the board, therefore, routes the signals using a microstrip line, and amplifies each signal by about 40 dB using two cascaded LNAs with a 2 dB Noise Figure and a 9 GHz bandwidth in the 9 to 18 GHz range. Moreover it compensates the phase delay by adding a line of proper length in one of the two brunches, and recombines the two outputs through a Wilkinson power combiner. Across the board, trimmers are used to control the biasing levels and tune the RF gains to the desired values.

3.2 Beam steering experimental results

The experimental setup employed to study the beam steering functionality of the presented photonics-based PSs is reported in Fig. 4. The BFN is composed of four PSs controlling the phase of an RF tone at 13 GHz. A four-channel real-time oscilloscope (RTO) is used to analyse the effect of the PSs implementing the BFN.

A continuous-wave laser at $\lambda_{cw} = 1558.1$ nm is modulated by a 13 GHz RF oscillator in a DPMZM, to obtain the single sideband modulated optical signal. After amplification by an EDFA, the optical signal is split to the four PSs in the BFN. The PSs are all calibrated to centre the filtering port of the ODF to the laser wavelength.

To steer a PAA beam towards an angle θ_0 , a phase difference $\Delta\theta_n$ shall be set at each n -th antenna element with respect to the first one; with $n \in [0, N-1]$. Considering elements spaced by a distance d :

$$\Delta\theta_n = \frac{2\pi}{\lambda} n \cdot d \cdot \sin \theta_n \quad (1)$$

where λ is the wavelength of the radiated RF signal [9].

The phase shift at each PS is controlled by an 80 MHz-BW arbitrary waveform generator (AWG) that is used for generating either constant or stepped voltages, allowing both the static and dynamic characterization of the BFN.

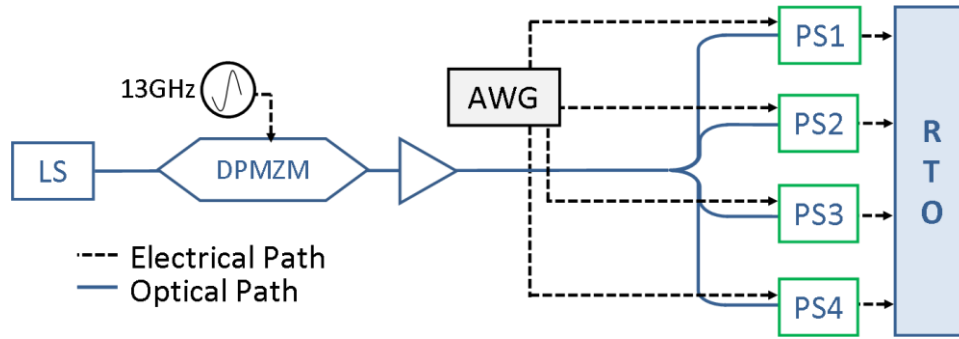


Figure 4. Setup of the beam steering experiment.

For the static characterization, power and phase responses of each PS element are measured by the VNA while gradually changing the DC voltage applied to the phase modulator in the PIC. The results are reported in Fig. 5 and are aligned with the PIC characterization reported in the previous section. Fig. 5a) shows the phase shift produced on the 13 GHz output RF signal by each circuit. The 4 curves exhibit a good linearity, with a phase variation in excess of 360° over less than 7 V. Fig. 5b) shows the power fluctuations induced on the RF signal by varying the control voltage: a power variation within ~ 4 dB is measured over a 360° phase shift. In fact, a change in the polarization of the p-n junction induces a change in its refractive index, i.e. on its transparency. This entails a variation of the attenuation of the optical signal propagating through the phase modulator; hence, the RF power variation. In the following, we evaluate how these power variations affect the beam emitted by a PAA.

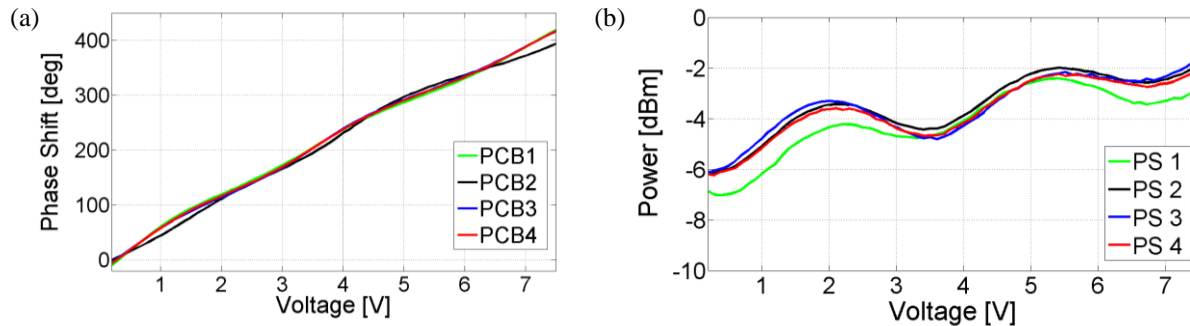


Figure 5. Characterization of the phase shift (a) and output power (b) of the four circuits, varying the voltage applied to the optical phase modulator.

The radiation pattern of a PAA can be obtained by multiplying the radiation pattern of the single element with the array factor $AF(\theta)$:

$$AF(\theta) = \sum_{n=0}^{N-1} a_n \exp \left[j \left(n \frac{2\pi}{\lambda} d \cdot \sin \theta - \Delta \theta_n \right) \right] \quad (2)$$

where θ is the view angle, N is the number of elements in the array, a_n is the relative amplitude of the current at the n -th element, d is the distance between adjacent element, and $\Delta \theta_n$ is the phase shift of each element with respect to the first one as given by Eq. (1). We use the AF to calculate the radiation pattern of a PAA driven by our PSs, considering the PAA pointing at $\theta_0 = 0^\circ$ and $\theta_0 = -60^\circ$. From Eq. (1), the set of phase shift to the four PSs are $[0^\circ, 0^\circ, 0^\circ, 0^\circ]$ and $[0^\circ, 156^\circ, 312^\circ, 108^\circ]$, for the two pointing angles respectively. The SFG generates two sets of voltages so that the phase shifts reported above are obtained at the four PSs.

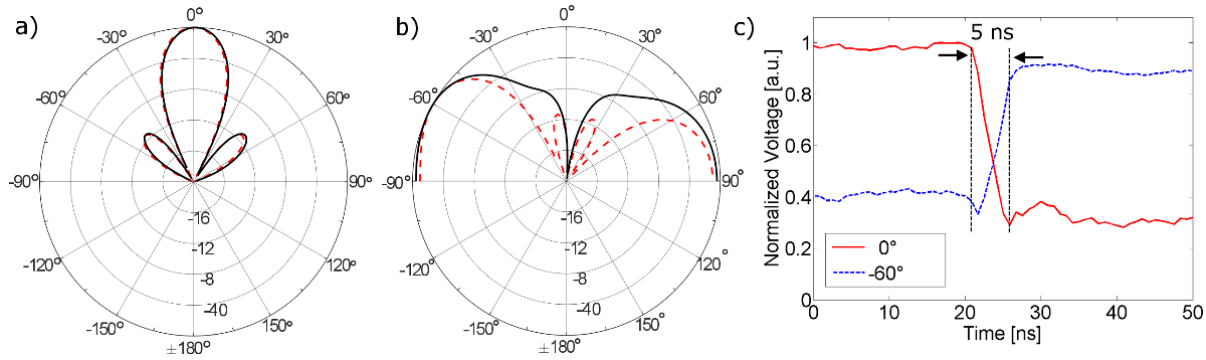


Figure 6. Comparison of ideal (dashed red lines) and real (solid, black lines) array factor diagrams for a PAA pointing at 0° (a) and at -60° (b). (c): Power emitted by the PAA as seen from view angles at 0° and -60° during the steering switch.

Considering four antenna elements spaced by $\lambda/2$, and setting $a_n = 1$, the AF of an ideal PAA pointing at 0° can be calculated as reported by the dashed red line in Fig. 6a). Instead, the AF of the photonics-based BFN is calculated by measuring on the oscilloscope the relative amplitude and actual phase shifts $\Delta\theta_n$ of each PS, for a steering angle $\theta_0 = 0^\circ$. The RF amplifiers on the PCBs have been first trimmed to emit the same RF amplitude. The obtained AF is represented by the solid black line of Fig. 6a). As expected, the ideal and real AFs coincide. Then, the phase settings are changed for pointing at $\theta_0 = -60^\circ$ while maintaining the same amplifier settings. The calculated AF is reported in Fig. 6b) compared with the ideal one. The curves for the ideal and real AF are in good agreement, both showing the maximum at -60°, but a difference in the shape can be recognized. This is due to the optical power fluctuations in the PSs studied in Fig. 6b). A modification of the PIC is already under study to suppress these fluctuations and hence improve the beam forming accuracy of the BFN.

In the dynamic characterization, the circuits are driven to simultaneously switch between the phase settings $\theta_0 = 0^\circ$ and $\theta_0 = -60^\circ$; their outputs are acquired by the RTO and processed. The red solid curve in Fig. 6c) shows the RF power behaviour seen from the view angle $\theta = 0^\circ$ during the steering from 0° to -60°, while the blue dashed curve reports the RF power observed at the same time from the view angle $\theta = -60^\circ$. The power behaviour clearly describes the effective steering of the PAA, changing quickly from a static condition at $\theta_0 = 0^\circ$ to a static condition at $\theta_0 = -60^\circ$. The power levels seen from $\theta = 0^\circ$ and -60° are not equal, as it would be expected, due to the power fluctuations discussed above. The time needed by the BFN to switch the beam between the two angles is about 5 ns, limited by the bandwidth of the available AWGs (80 MHz).

4. CONCLUSIONS

A photonic integrated microwave phase-shifter has been realized in CMOS-compatible SOI technology. The device operation is based on carrier-sideband isolation from a full-carrier single-sideband modulated signal in an optical deinterleaver filter and on the processing of the optical carrier phase alone in an optical phase shifter. The circuit characterization confirmed wide phase shifts in excess of 360° and a precision below 0.1°/mV. The flat-top characteristic of the periodic deinterleaver passband window also permits flexible choice of the RF carrier, and broadband operation over a typical bandwidth of 6 GHz is demonstrated. Additionally, by implementing the optical phase shifter in a p-n junction silicon rib waveguide exploiting fast carrier-depletion modulation effect, a small reconfiguration time of about 1 ns is achieved, which outperforms previous realizations in SOI technology based on thermo-optic effect. The integration of germanium photodiodes provides improved chip functionality, by enabling the access of the phase-shifted microwave signal through electrical contacts, which ease the packaging of the device for practical system applications.

Four PICs have been packaged and mounted on dedicated PCBs, allowing their easy utilization and implementation in an actual BFN. The performance of the BFN confirms the suitability of the approach for future PAAs. In particular, the range, speed and precision of the achievable phase shift promise the implementation of satellite-tracking PAAs as well as user specific beam forming.

ACKNOWLEDGMENT

The Authors thank A. D'Errico and M. Puleri from Ericsson Telecomunicazioni SpA for the fruitful discussions. This activity has been supported by the projects H2020 ROBORDER (#740593), NATO SPS SOLE, and National Projects PREVENTION and PHOOD.

REFERENCES

- [1] D.B. Adams, and C.K. Madsen, "A novel broadband photonic RF phase shifter", *J. Lightwave Technol.*, vol. 26, no. 15, pp. 2712–2717, Aug. 2008.
- [2] M. Pu *et al.*, "Widely tuneable microwave phase shifter based on silicon-on-insulator dual microring resonator", *Opt. Expr.*, vol. 18, no. 6, pp. 6172–6182, Mar. 2010.
- [3] G. Serafino *et al.*, "Design and characterization of a photonic integrated circuit for beam forming in 5G wireless networks", 2017 International Topical Meeting on Microwave Photonics (MWP), Beijing, 2017, pp. 1–4.
- [4] M. Burla *et al.*, "On-chip CMOS compatible reconfigurable optical delay line with separate carrier detuning for microwave photonic signal processing", *Opt. Expr.*, vol. 19, no. 22, pp. 21475–21484, Oct. 2011.
- [5] R.A. Soref, and B.R. Bennett, "Electrooptical effects in silicon", *IEEE J. Quantum Electron.*, vol. 23, no. 1, pp. 123 – 129, Jan. 1987.
- [6] V.J. Urick *et al.*, "Microwave phase shifting using coherent photonic integrated circuits", *IEEE J. Sel. Topics Quant. El.*, vol. 22, no. 6, Dec. 2016.
- [7] "Europractice MultiProject Wafer", www.europractice.ic.com/SiPhotonics_technology_imec_ISIPP25G.php
- [8] K. Oda, N. Takato, H. Toba, and K. Nosu, "A wide-band guided-wave periodic multi/demultiplexer with a ring resonator for optical FDM transmission systems", *J. Lightwave Technol.*, vol. 6, no. 6, pp. 1016–1023, June 1988.
- [9] M. Longbrake, "True time-delay beamsteering for radar", NAECON 2012, Dayton, Ohio, USA, July 2012.